Strain-induced majority carrier inversion in ferromagnetic epitaxial $LaCoO_{3-\delta}$ thin films

Vipul Chaturvedi,[1] Jeff Walter,[1,2] Arpita Paul,[1] Alexander Grutter,[3] Brian Kirby,[3] Jong Seok Jeong,[1] Hua Zhou,[4] Zhan Zhang,[4] Biqiong Yu,[5] Martin Greven,[5] K. Andre Mkhoyan,[1] Turan Birol,[1] and Chris Leighton[1,*]

[1]*Department of Chemical Engineering and Materials Science, University of Minnesota, Minneapolis, Minnesota 55455, USA*
[2]*Department of Physics, Augsburg University, Minneapolis, Minnesota 55454, USA*
[3]*NIST Center for Neutron Research, NIST, Gaithersburg, Maryland 20878, USA*
[4]*Advanced Photon Source, Argonne National Laboratory, Lemont, Illinois 60439, USA*
[5]*School of Physics and Astronomy, University of Minnesota, Minneapolis, Minnesota 55455, USA*

(Received 28 October 2019; revised manuscript received 17 January 2020; accepted 5 February 2020; published 4 March 2020)

Tensile-strained $LaCoO_{3-\delta}$ thin films are ferromagnetic, in sharp contrast to the zero-spin bulk, although no clear consensus has emerged as to the origin of this phenomenon. While magnetism has been heavily studied, relatively little attention has been paid to electronic transport, due to the insulating nature of the strain-stabilized ferromagnetic state. Here, structure, magnetism, *and* transport are studied in epitaxial $LaCoO_{3-\delta}$ films (10–22-nm thick) on various substrates (from 1.4% compressive to 2.5% tensile strain), using synchrotron x-ray diffraction, scanning probe and transmission electron microscopy, magnetometry, polarized neutron reflectometry, resistivity, and Hall effect. High quality, smooth films are obtained, exhibiting superstructures associated with both oxygen vacancy ordering and periodic in-plane ferroelastic domains. Consistent with prior work, ferromagnetism with an approximately 80–85 K Curie temperature is observed under tension; polarized neutron reflectometry confirms a relatively uniform magnetization depth profile, albeit with interfacial dead layer formation. Electrical transport is found to have similar semiconducting nature to bulk, but with reduced resistivity and activation energy. Hall effect measurements, however, reveal a striking inversion of the majority carrier type, from *p*-type in the bulk and under compression to *n*-type under tension. While thus far overlooked, ferromagnetism in epitaxial $LaCoO_{3-\delta}$ films is thus directly correlated with *n*-type behavior, providing important insight into the ferromagnetic state in this system. Aided by density functional theory calculations, these results are interpreted in terms of tensile-strain-induced orbital occupation and band structure changes, including a rapid decrease in effective mass at the e_g-derived conduction band minimum, and corresponding increase at the valence band maximum.

DOI: 10.1103/PhysRevMaterials.4.034403

I. INTRODUCTION

Complex transition metal oxides such as perovskites exhibit a delicate interplay among structural, orbital, charge, and spin degrees of freedom, often in the presence of strong electronic correlations and/or spin-orbit coupling [1–4]. The varied electronic and magnetic ground states of these materials can thus be highly susceptible to perturbations, heteroepitaxial strain being a prime example. Growth of fully strained (i.e., pseudomorphic) perovskite films on substrates with tensile or compressive lattice mismatch of up to several percent has yielded many advances [1–4], including strain stabilization of ferroelectricity in quantum paraelectric $SrTiO_3$ [5,6], multiferroicity in strained $EuTiO_3$ [7], and the many examples of strain-tuned magnetism in manganite-based films and heterostructures [8].

The 2007 discovery of ferromagnetism (FM) in tensile-strained films of $LaCoO_{3-\delta}$ (LCO) provided a particularly intriguing example of a strain-induced ground state radically different from bulk [9]. Due to the slight dominance of the crystal field splitting (Δ_{CF}) over the Hund exchange energy (H_{ex}), Co^{3+} ions in bulk rhombohedral ($R\bar{3}c$ [10,11]) LCO adopt a zero-spin ground state [the $t_{2g}{}^6e_g{}^0$, $S = 0$, low spin (LS) state], resulting in *diamagnetism* [10–27], in stark contrast to FM in tensile-strained films. Warming bulk LCO to as little as 30 K populates nonzero spin states, simplistically labeled intermediate spin (IS, $t_{2g}{}^5e_g{}^1$) or high spin (HS, $t_{2g}{}^4e_g{}^2$) [10–27]. This 30–80 K thermally excited spin-state transition, or spin crossover, has been extensively studied in LCO, both experimentally [10–13,15–20,23–25], and theoretically [14,21,22,26,27], although the exact nature of the excited spin state remains controversial. This is likely in part due to the inappropriateness of description via atomic states such as LS, IS, and HS (given the substantial Co e_g–O $2p$ hybridization) [26], as well as the need to account for spin-orbit coupling [21,22]. At higher temperature (T), around 500 K, a broad insulator-metal transition occurs in bulk LCO, accompanied by a second change in spin state [15–18,20]. The nature of this transition is also not clear, although melting of orbital order [16] and a Mott insulator to metal transition are possible [18].

While the spin-state transition/crossover of Co^{3+} ions in bulk LCO is well established, reports of weak FM phenomena

*Corresponding author: leighton@umn.edu

at low T, in the nominally $S = 0$ (LS) diamagnetic ground state, are nevertheless common [28–34]. Defect-driven magnetism is thought to occur, including surface FM [29], weak FM associated with magnetic excitons/spin-state polarons forming around oxygen vacancies (V_O) [28,30,31,33] and enhanced magnetism in fine particles [34]. Perhaps unsurprisingly given the delicate balance between Δ_{CF}, H_{ex}, and Co e_g–O $2p$ hybridization, the spin state and magnetic order in LCO are thus extremely sensitive to perturbations such as surfaces and interfaces [29,34], line defects [32], point defects [28,30,31,33] and strain [9]. LCO has therefore emerged as an important system in which to study the interplay among magnetism, structure, disorder, defects, etc., epitaxial films being of particular interest.

Many publications since 2007 have documented the physical properties of strained epitaxial LCO, seeking to understand the FM ground state. While magnetism has been detected under both tensile and compressive heteroepitaxial strain, tensile strain strongly favors FM [35,36], polycrystalline films being non-FM [9]. Typical Curie temperatures, saturation magnetizations, and low T coercivities reach $T_C \approx 80$–95 K, $M_s \approx 0.5$–$1.0\,\mu_B$/Co, and $H_c \approx 5$ kOe (4×10^5 Am^{-1}) under 1–2% tensile strain [9,32,35–49]. It should be noted, however, that nonsaturation of the magnetization is sometimes apparent [9,36,47,49] and that M_s up to $\sim 2\,\mu_B$/Co has been reported [36,47,49]. Magnetic force microscopy confirms long-range FM under tension, while only short-range FM is seen under compression [38]. As expected from the observation of FM, suppression of the transition to the LS state at low T has been reported based on x-ray absorption spectroscopy (XAS) [50]. The IS state, HS state, and various ordered and disordered combinations have in fact been claimed in tensile-strained LCO films, from XAS [36,50,51], near-edge x-ray absorption fine-structure (NEXAFS) [39,50,51], x-ray absorption near-edge spectroscopy (XANES) [39], x-ray magnetic circular dichroism [36,47,49,51], x-ray magnetic linear dichroism [47,49], extended x-ray absorption fine structure (EXAFS) [39], resonant inelastic soft x-ray scattering [46], and scanning transmission electron microscopy/electron energy loss spectroscopy (STEM/EELS) [32,36]. Such spectroscopies provide strong evidence for orbital occupancy redistributions consistent with strain-induced nonzero spin states [36,39,46,47,50], although XAS data have also been interpreted in terms of doping due to nonstoichiometry [37].

In terms of structure, probes such as laboratory x-ray diffraction (XRD), TEM, STEM/EELS, and synchrotron x-ray diffraction (SXRD) have revealed a wealth of observations, across multiple scales. Thickness (t)-dependent XRD studies highlighted the importance of tetragonal distortions in tensile-strained LCO films, the bulklike rhombohedral distortions at high t leading to reduced M_s [52]. Related to this, an intriguing periodic in-plane domain structure has been observed (via TEM and XRD rocking curves) in LCO films on cubic substrates such as $(LaAlO_3)_{0.3}(SrAl_{0.5}Ta_{0.5}O_3)_{0.7}$ (LSAT), with a 1.5% tensile pseudocubic lattice mismatch [52]. Similar phenomena occur in some manganite films [53], the understanding being that at sufficient thickness a periodic in-plane twin domain structure develops, due to the lower symmetry of the film relative to the substrate, i.e., ferroelasticity. Even below 200 Å, LSAT(001)/LCO films present an in-plane modulation with approximately 100 Å periodicity, thought to be a precursor to the full ferroeleastic twin domain state. At a shorter length scale, cross-sectional STEM studies since 2012 have evidenced local lattice modulations in the form of atomic-scale stripe patterns. These patterns were originally interpreted as a lattice and spin-state superstructure [40], although similar stripes were observed in Sr-doped LCO where they were definitively assigned to V_O order [54–56]. In the Sr-doped LCO case the V_O order has been established as the primary lattice mismatch accommodation mechanism in heteroepitaxial films, the V_O order orientation (e.g., in-plane vs perpendicular stripes) being controllable via lattice mismatch [55]. Later STEM work on LCO directly observed O content modulation via EELS, confirming V_O order as the origin of the stripes in LCO as well [32]. Strong correlations between the extent of V_O order and FM were then found in LCO films [36]. Simultaneous with this, resonant SXRD studies uncovered yet another structural modulation in tensile LCO films [41,44]. Fujioka *et al.* detected a clear structural change below 126 K in films on LSAT, corresponding to quadrupling of the unit cell [41]. This was interpreted in terms of an IS/HS spin-orbital superstructure, leading to *ferri*magnetism. Later work established strain dependence to both the transition temperature and modulation vector [44]. Depth-resolved studies of structure and magnetism have also been performed on LCO films, using grazing-incidence x-ray reflectivity (GIXR) and polarized neutron reflectometry (PNR) [48]. The primary findings include an interfacial tetragonally-distorted phase sandwiching a lower symmetry monoclinic phase, with related variations in M_s [48]. Aside from this, the magnetization was found to be relatively uniform with depth, confirming bulk FM.

Based on these findings, multiple explanations have been advanced for the FM in tensile-strained LCO. Strain stabilization of nonzero spin states appears well established, although, much like bulk LCO at high T, the nature of the nonzero spin states is less clear. That tensile strain, expanded Co–O bonds, and closer to 180° Co–O bond angles should increase the e_g-derived bandwidth and lower Δ_{CF}, thus favoring higher e_g occupation and nonzero spin states, has been pointed out since the earliest work [9]. Such factors are directly linked to suppression of bulklike rhombohedral distortions and stabilization of strain-induced tetragonal ones [52]. On the basis of XAFS and XANES, Sterbinsky *et al.* in fact claimed that such distortions are more important than changes in Co-O bond lengths and hybridization [39]. Later work establishing the various superstructures discussed above led to more nuanced proposals for the nonzero spin states, focusing on spin-state superstructures. Resonant SXRD results have been interpreted in terms of both an ordered HS/LS checkerboard [45] and an HS/IS spin-orbital superstructure [41,44]. With the assistance of density functional theory (DFT) calculations, the STEM/EELS results on V_O ordering were similarly interpreted in terms of Co^{3+}/Co^{2+} spin-state superstructures, including an HS/LS checkerboard [32], and more complex possibilities [43]. One advantage of such spin-state superstructures is that they are consistent with the fairly low, and variable, M_s. In terms of spin *coupling*, superexchange among the various species in these spin-state superstructures has been emphasized [57], along with increased e_g population [39,51],

which may favor FM, as in doped LCO (e.g., $La_{1-x}Sr_xCoO_3$ [58]).

DFT first-principles electronic structure calculations have also been applied to tensile-strained LCO [32,57,59–61]. Early work by Rondinelli and Spaldin [59] and Gupta and Mahadevan [60] pointed out that FM due to IS Co^{3+} is readily stabilized under tension, modification of the Co-O octahedral symmetry playing a key role [59]. Later work considered spin-state superstructures [61], the superexchange-coupled HS/LS ordered state, which was claimed to be the lowest energy configuration, featuring prominently [32,57,61]. This state was also found to be insulating [57,61], as was the Co^{3+}/Co^{2+} spin-state superstructure deduced from STEM/EELS and DFT [32]. This is significant, as calculations on the pure IS state predict metallicity [59], at odds with experiment [37,42,62]. To summarize, while uncertainty remains with respect to the nature of the tensile-strain-induced nonzero spin states, there is agreement, both experimentally and theoretically, that redistribution of Co orbital population occurs under tension in LCO, favoring FM.

A notable feature of the FM state in tensile-strained epitaxial LCO films is its nonmetallic character. Thin film LCO is in fact sufficiently resistive that few studies have included electronic transport measurements, those that do probing only a modest T range. In 2008 Freeland *et al.* reported 300 K resistivity (ρ) of 10–100 Ωcm on $SrTiO_3$ (STO) and $LaAlO_3$ (LAO) substrates, with strongly insulating behavior down to approximately 100 K [37]. Rivadulla *et al.* reported similar findings in LCO on STO, along with negative magnetoresistance just below T_C [42]. In 2016, Liu *et al.* then reported 1–100 Ωcm 300 K resistivities, again measurable only to about 100 K [62]. Particularly in light of the very different magnetism, these transport properties are remarkably similar to bulk. The 300 K ρ of bulk LCO varies somewhat (likely due to doping from unintentional nonstoichiometry and impurities), but the transport is clearly insulating below the 500 K metal-insulator transition [15–18,20]. This is consistent with the semiconducting character of bulk LCO from optical measurements [15,18] and DFT [14,26,27], although uncertainty remains over the true band gap [15,18]. Regarding conduction mechanisms, the lowest T transport study available (English *et al.* [20]) reported a change in activation energy of the bulk resistivity of LCO below 80 K (from 150 to 40 meV), coincident with the spin-state transition. Magnetotransport measurements revealed an accompanying crossover from anisotropic positive magnetoresistance due to hopping at low T, to isotropic negative magnetoresistance associated with thermally excited spin disorder at higher T, directly reflecting the spin-state transition [20]. In terms of the Hall effect, nominally undoped single crystal LCO is reported to exhibit holelike (p-type) transport, with deduced mobility of $0.03\,cm^2\,V^{-1}\,s^{-1}$ at 340 K [18]. Significantly, it is not known how such magnetotransport properties translate to films, how they respond to strain, or how they correlate with FM. Although high ρ hampers measurements, particularly over wide T ranges, much could thus be learned from more detailed transport studies on high quality LCO films.

Motivated by the above, here we report a systematic study of not only magnetism but also electronic transport in LCO films grown on STO, LSAT, LAO, and $SrLaAlO_4$ (SLAO) substrates, generating lattice mismatches from +2.49% (tensile) to −1.42% (compressive). Films with $t = 100$–220 Å grow nominally fully strained to the substrates, SXRD evidencing single-phase epitaxy and the previously observed periodic in-plane superstructure. GIXR and atomic force microscopy (AFM) indicate low (unit-cell-level) surface roughness, while STEM reveals strain-induced V_O order. As expected, tensile strain results in FM with T_C of approximately 80–85 K, PNR confirming relatively uniform magnetization depth profiles, albeit with interfacial dead layers. In terms of transport, $\rho(T)$ is found relatively similar to bulk, but with reduced resistivities and activation energies. Hall measurements, however, reveal a clear sign reversal of the ordinary Hall coefficient in tensile-strained films. Both the magnitude of the carrier mobility and the form of $\rho(T)$ rule out factors such as variable-range hopping conduction, confirming inversion of the majority carrier type, from p-type in the bulk and under compression, to n-type under tension. While this has thus far escaped attention, the FM in tensile-strained LCO films is therefore directly correlated with n-type transport. Complementary DFT reveals that the electron effective mass at the conduction band minimum decreases by a factor of about 4 from compression to tension, while the hole effective mass at the valence band maximum rises by a factor of about 2. The ratio of electron to hole masses thus drops by almost an order of magnitude under tensile strain, providing, along with strain-induced changes in orbital population, a viable explanation for the observed n-type conduction.

II. EXPERIMENTAL AND COMPUTATIONAL METHODS

LCO films with $100\,Å < t < 220\,Å$ were grown by high pressure oxygen sputter deposition using methods similar to Sr-doped LCO [63]. Immediately prior to growth, commercial substrates were annealed at 900 °C in 1 Torr (130 Pa) of flowing O_2 for 15 mins. Substrates were then cooled to 700 °C for growth in 1.5 Torr (200 Pa) of ultra-high-purity O_2, at 64 W of DC sputter power, from a 5-cm diameter nominally stoichiometric LCO ceramic target synthesized by solid-state reaction. This results in deposition rates around 10 Å/min. After growth, films were cooled at approximately 15 °C/min in 600 Torr (8×10^4 Pa) of O_2. Bulk LCO has a 300 K pseudocubic lattice constant (a_{pc}) of 3.810 Å [64], resulting in compressive lattice mismatch on SLAO (−1.42%) and LAO (−0.55%), and tensile mismatch on LSAT (1.52%) and STO (2.49%).

GIXR was performed on a Panalytical X'Pert system (Cu K_α) to determine film thicknesses and density depth profiles. SXRD was done at 300 K on the 33-ID beamline of the Advanced Photon Source, using 20 keV (0.62 Å) radiation. Film surface morphology was studied using contact-mode AFM on a Bruker Nanoscope V Multimode 8. High-resolution STEM employed an abberation-corrected FEI Titan G2 60–300 STEM operated at 200 kV. Cross-sectional STEM specimens were prepared with a focused ion beam (FEI Helios NanoLab G4) using 30 kV Ga ions, followed by 1–5 kV ion milling to remove damaged surface layers. The STEM probe convergence semiangle was 23.5 mrad and the high-angle annular dark-field (HAADF) detector inner angle was 57 mrad. Magnetometry measurements employed a Quantum Design

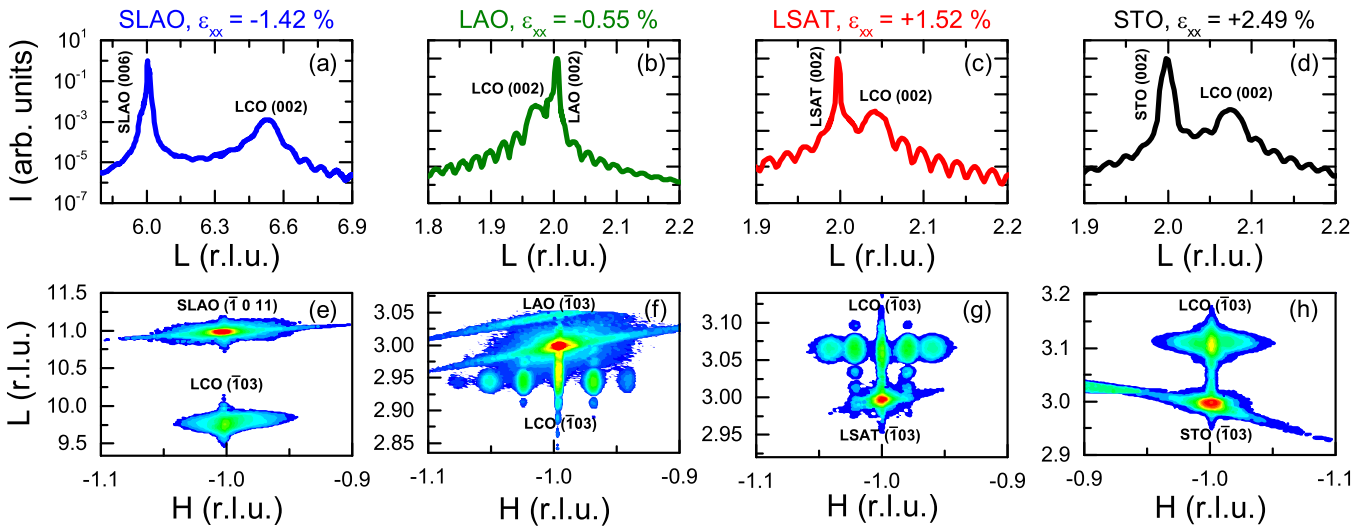

FIG. 1. Specular synchrotron x-ray diffraction scans around the film 002 reflections of 190-Å-thick $LaCoO_{3-\delta}$ (LCO) films on (a) SLAO, (b) LAO, (c) LSAT, and (d) STO substrates. In-plane strains (ε_{xx}) are labeled. (e)–(h) Corresponding synchrotron x-ray reciprocal space maps around the asymmetric $\bar{1}03$ film reflections ($\bar{1}$ 0 11 for SLAO) for the same films shown in (a)–(d). "r.l.u." is used for (substrate) reciprocal lattice units.

superconducting quantum interference device magnetometer, operated between 5 and 300 K in in-plane magnetic fields (H) to 70 kOe (5.6×10^6Am^{-1}). For magnetization depth profiling, PNR was performed at 5 K on the Polarized Beam Reflectometer at the NIST Center for Neutron Research, using a monochromated beam (4.75 Å) and a saturating (30 kOe, 2.4×10^6 Am^{-1}) in-plane magnetic field. The normal scattering vector (Q) dependence of the two nonspin-flip specular reflectivities, R^{++} and R^{--}, were measured, where "+" and "−" refer to incoming and outgoing neutron spin polarization parallel or antiparallel to the applied field. $R(Q)$ was modeled with the NIST Refl1D software [65], using the DREAM Markov chain Monte Carlo algorithm implemented in the BUMPS package to determine uncertainty estimates on fitted parameters. To minimize the number of parameters in the refinement of magnetic depth profiles, 200-K unpolarized neutron reflectometry data were also taken (in addition to GIXR), to establish the chemical depth profile. DC transport measurements were done in a Quantum Design Physical Property Measurement System from 50 to 400 K in fields to 90 kOe (7.2×10^6 Am^{-1}). A Keithley 220 current source and a Keithley 2002 voltmeter were used for excitation and measurement. Indium contacts in a van der Pauw geometry were used, with frequent checks for nonohmicity and self-heating.

Electronic structure calculations employed DFT, using the projector augmented wave approach, as implemented in VASP [66]. The exchange correlation energy was calculated within the Perdew-Burke-Ernzerhof (PBE)sol [67] approximation. An energy cutoff of 500 eV was used to truncate the plane-wave basis set and a $4\times4\times4$ k-point grid was used to integrate over the Brillouin zone. A Hubbard U correction was included [68], to account for on-site interaction among d electrons in Co^{3+}. As in prior literature on cobaltites, a large value of U ($U = 6$ eV) was required [61] to obtain quantitative agreement with the bulk crystal structure [11,64], while $U = 3$ eV was sufficient to obtain electronic structure in agreement with experiment [15,18]. As the key issue here is the strain dependence of the crystal and band structure, spin polarization was not included. Biaxial strain was imposed by constraining the in-plane lattice parameters and then relaxing the structure; optimizations used the condition that the Hellman-Feynman forces fall below 5 meV Å^{-1}. 40-atom $2\times2\times2$ supercells were employed to accommodate the various strain-induced CoO_6 octahedral rotation patterns. For analysis of trends in orbital energies, the WANNIER90 package [69,70] was used to calculate maximally localized Wannier functions. A tight-binding model with 2 e_g orbitals per Co was then constructed, using an inner window spanning the lowest 3.7 eV of the conduction band.

III. RESULTS AND ANALYSIS

A. Structural characterization

Shown in Figs. 1(a)–1(d) are specular SXRD scans (intensity (I) vs L in reciprocal lattice units [(r.l.u.)] around the 002 film peaks from 190-Å-thick LCO films on SLAO(001), LAO(001), LSAT(001), and STO(001). Only the allowed 00l LCO peaks are observed (even over a broader Q range than shown here), indicating phase purity within SXRD detection limits, and out-of-plane epitaxy. Numerous Laue oscillations are seen, demonstrating low roughness, as confirmed by GIXR, AFM, and PNR. Film thicknesses extracted from Laue oscillations, the widths of the specular 002 peaks, and GIXR (not shown) are in excellent agreement, as expected for fully strained (i.e., microstrain-free) films. The pseudomorphic nature of the films at this t is confirmed by the reciprocal space maps (RSMs) shown in Figs. 1(e)–1(h), which were taken around asymmetric $\bar{1}03$ reflections. The film and substrate share the same in-plane lattice parameters (i.e., they diffract at the same H), but distinctly different out-of-plane lattice parameters (i.e., different L), as expected for full strain.

Interestingly, the SXRD RSMs in Figs. 1(f)–1(g), on LAO and LSAT, reveal an additional rich structure of satellite peaks.

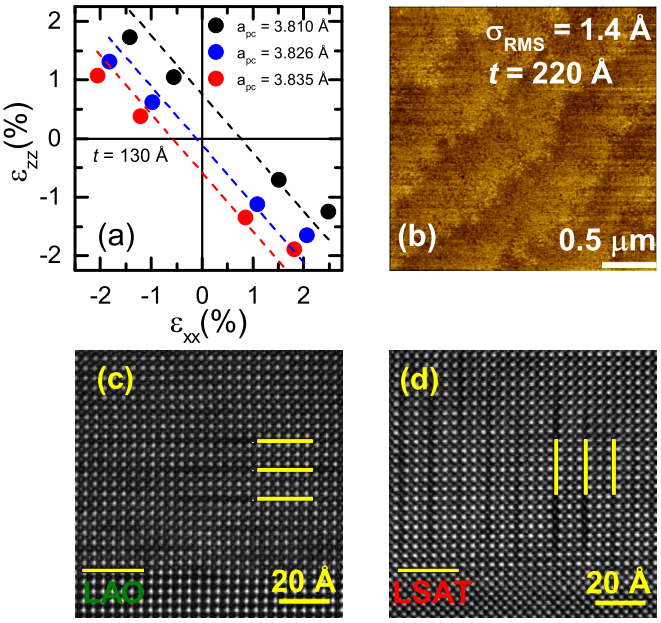

FIG. 2. (a) Out-of-plane strain (ε_{zz}) vs in-plane strain (ε_{xx}) for 130-Å-thick $LaCoO_{3-\delta}$ films, assuming various values [35,36,52] for the bulk pseudocubic lattice parameter (a_{pc}). The dashed lines are straight-line fits with unity slope, corresponding to Poisson ratio 1/3. (b) Contact mode atomic force microscopy image (2.5×2.5 μm) of a 220-Å-thick $LaCoO_{3-\delta}$ film on LAO, showing the extracted RMS roughness. HAADF-STEM images of 100-Å-thick $LaCoO_{3-\delta}$ films on (c) LAO and (d) LSAT. Yellow horizontal or vertical lines highlight the oxygen vacancy ordering orientation.

On LSAT(001), for example [Fig. 1(g)], the film $\bar{1}03$ reflection has two clear satellites on either side of the main Bragg peak, evenly spaced in H, those satellites having Laue oscillations. Similar behavior is seen on LAO(001) [Fig. 1(f)], the in-plane satellites again being periodic, and extending even to third order. On SLAO(001) and STO(001), however [Figs. 1(e)–1(h)], this behavior disappears, replaced with wide streaks of scattering around the LCO $\bar{1}03$ reflection, along H. As noted in the Introduction, this type of behavior has been detected in 00l rocking curves of LSAT(001)/LCO [52], although the use of SXRD reciprocal space maps here provides higher sensitivity and a broader view (we also study $\bar{1}03$ vs 00l reflections). Fuchs *et al.* interpreted this behavior in terms of a periodic in-plane structural modulation, at these thicknesses essentially a precursor to a periodic in-plane ferroelastic twin domain structure due to the lower symmetry of LCO (rhombohedral) than the substrate (cubic) [52]. Similar ideas have been advanced for $La_{1-x}Sr_xMnO_3$ on STO [53]. Fuchs *et al.* also observed the periodic twin domain structure in both cross-sectional and plan-view TEM on LSAT(001)/LCO [52]. Following their interpretation, the LSAT(001)/LCO data in Fig. 1(g) yield a periodic in-plane modulation distance of 95 Å (from the satellite spacing in H), an equivalent correlation length of 105 Å (from the satellite width in H), and an out-of-plane length scale of 130 Å from the finite size fringe spacing along L. These values indicate a somewhat coherent in-plane modulation, with wavelength in good agreement with Fuchs *et al.* at this t. The out-of-plane length scale of 130 Å also fits with the Fuchs *et al.* picture, the fact that it is less than the thickness (190 Å) indicating that a thin LCO region near the substrate likely deforms without lateral modulation. On LAO(001) we extract a similar wavelength of 70 Å. Note that in this case the symmetry of LAO and LCO is the same ($R\bar{3}c$) at 300 K, but not at the 700 °C growth temperature, where LAO should be cubic (bulk LAO transforms to $Pm\bar{3}m$ at 540 °C [71]). The symmetry mismatch twin domain interpretation thus may also be applicable to LAO(001)/LCO. The replacement of distinct satellite peaks with a broad streak of scattering in films on SLAO(001) and STO(001) [Figs. 1(e) and 1(h)] could then potentially indicate decreased coherence of the in-plane modulation at higher absolute lattice mismatches. (Note that some films on STO do exhibit weak satellites around certain reflections, consistent with Guo *et al.* [49]; the coherence of the in-plane modulation is stronger on LAO and LSAT, however.)

A final point worth emphasizing along these lines is that the in-plane ferroeleastic domain structure in LCO [52] has apparently never been linked to the V_O order that is also reported in strained LCO films [32,36], and seen here (see below). It seems possible that lateral domains associated with this V_O order, which occur on length scales comparable to the 100 Å wavelengths deduced above, could also be responsible for the periodic in-plane domain structure seen in XRD rocking curves, RSMs, and TEM. Future work exploring this potential connection would be worthwhile.

With the in-plane and out-of-plane lattice parameters of these LCO films known, and full strain established, the strain components ε_{xx} and ε_{zz} can be determined, using $\varepsilon_{xx} = (a_{sub}–a_{pc})/a_{pc}$ and $\varepsilon_{zz} = (c–a_{pc})/a_{pc}$, where a_{sub} is the substrate (pseudo)cubic lattice parameter, a_{pc} is the LCO bulk pseudocubic lattice parameter, and c is the out-of-plane lattice parameter of the pseudotetragonal LCO film. These strains are plotted against each other in Fig. 2(a) at a fixed low t of 130 Å. For better comparison to prior literature this is done assuming a_{pc} values of 3.810, 3.826, and 3.835 Å, as used in Refs. [36], [52], and [35]. This range of LCO bulk a_{pc} values was used in past work to consider not only the 300 K value [64], but also values that reflect thermal expansion at the growth temperature [35]. For simple analysis, the dashed lines in Fig. 2(a) are straight line fits with unity slope, corresponding to a Poisson ratio of 1/3, as has been reported for both bulk LCO and epitaxial films [35]. The intermediate $a_{pc} = 3.826$ Å value of Fuchs *et al.* [52] is seen to generate the expected near-zero intercept; a 300 K a_{pc} value of 3.810 Å would instead indicate a substantial positive intercept along ε_{zz}, indicating additional expansion of the cell volume. The latter can occur in perovskites, including $La_{1-x}Sr_xCoO_{3-\delta}$, due to defects such as V_O [72].

Moving to microscopy, the 2.5×2.5 μm AFM image of a representative $t = 220$ Å LCO film on LAO(001) in Fig. 2(b) reveals atomically flat terraces separated by unit-cell-high steps. The root-mean-square (RMS) roughness from this image is 1.4 Å, consistent with the low (Å scale) roughness indicated by SXRD, GIXR, and PNR. Complementary cross-sectional STEM images are shown in Figs. 2(c) and 2(d) for representative 100-Å-thick LCO films on LAO(001) and LSAT(001), respectively. As reported previously [32,36,40,43], and as discussed in the

Introduction, atomic-scale stripe patterns are detected. Following the work of Biskup *et al.* [32] and Mehta *et al.* [36], which directly detected O deficiency in dark stripes using STEM/EELS, and consistent with the Sr-doped LCO film literature [54–56], we interpret this as V_O order. Different from the $x = 0.5$ $La_{1-x}Sr_xCoO_{3-\delta}$ case, but consistent with prior work on LCO, the stripe spacing is not a single pseudocubic unit cell, but rather three, or even four pseudocubic cells, with spatial variations. The stripes of V_O order (analogous to the O-deficient planes in V_O-ordered brownmillerite $SrCoO_{2.5}$ [54–56]) are also oriented in-plane on LAO(001) [Fig. 2(c)], but out-of-plane on LSAT(001) [Fig. 2(d)]. These observations are broadly consistent with heteroepitaxial $La_{1-x}Sr_xCoO_{3-\delta}$ films, where V_O ordering is thought to be the mechanism for lattice mismatch accommodation [55]. Specifically, in-plane (perpendicular) stripes are anticipated under compression (tension), to enable the V_O-ordered structure to lattice match the substrate, as in Figs. 2(c) and 2(d). The less prevalent V_O order on LAO [Fig. 2(c)] may be consistent with the smaller absolute lattice match than on LSAT(001) [Fig. 2(d)]. It should be noted, however, as will be returned to in Sec. IV below, that V_O order, and thus finite δ in $LaCoO_{3-\delta}$, is apparent here under both tensile and compressive strain.

B. Magnetism

Moving to magnetic properties, Fig. 3(a) shows the T dependence of the magnetization (M) of representative 150-Å-thick LCO films on SLAO, LAO, LSAT, and STO, measured (and cooled) in $H = 1$ kOe (8×10^4 Am^{-1}, in-plane). Consistent with expectations from the literature [9,35–38,41,42,47,49,52], FM ordering is apparent under tensile strain (on LSAT and STO), but not compressive strain (on SLAO and LAO). T_C values of 78 and 83 K are estimated from the inflection points of $M(T)$ for films on STO and LSAT, respectively. While both FM transitions are relatively sharp, films on LSAT do appear to have less broadened transitions, in addition to slightly higher T_C. On a qualitative level, comparison of Figs. 1(g), 1(h) and Figs. 3(a), 3(b) suggests that the higher T_C on LSAT compared to STO correlates with the somewhat higher structural quality on LSAT substrates (i.e., improved coherence of periodic in-plane modulation). Complementary in-plane 5 K $M(H)$ hysteresis loops of films on LSAT and STO [Fig. 3(b)] reveal clear hysteresis and in-plane magnetization. Coercivity (H_c) near 5 kOe (4×10^5Am^{-1}) is found on both substrates, the M_s values on LSAT and STO being 1.1 and 1.0 μ_B/Co, respectively. The T_C, M_s, and H_c values reported here are thus in reasonable quantitative agreement with the majority of the literature, e.g., Refs. [9,35,37,38,41,44]. As an aside, we note that a substantial nonlinear paramagnetic signal was found to arise in LSAT substrates at low T, which had to be carefully subtracted. If not accounted for this could lead to anomalously large deduced M_s, and a lack of saturation out to high H.

PNR was used to further probe the magnetism in tensile-strained LCO films on STO and LSAT substrates, to confirm long-range bulk FM order, and to quantify the magnetization depth profile. Figures 4(a) and 4(d) show the Q dependence of the nonspin-flip specular reflectivities R^{++} and

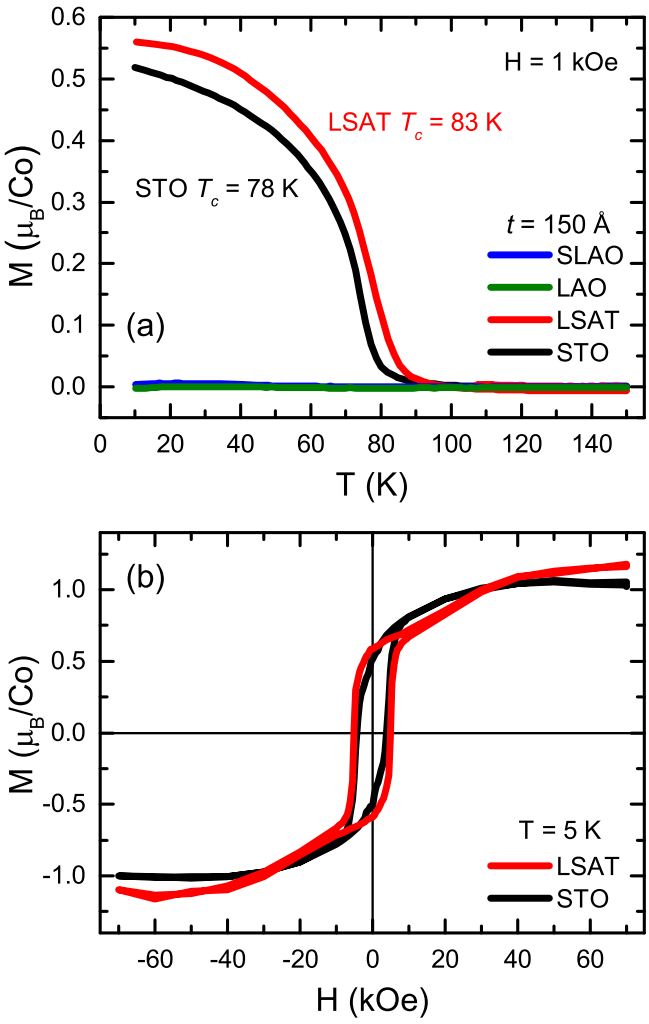

FIG. 3. (a) Temperature (T) dependence of magnetization (M) of 150-Å-thick $LaCoO_{3-\delta}$ films on various substrates at 1 kOe (8×10^4 Am^{-1}) in-plane measuring and cooling field. (b) M vs in-plane magnetic field (H) at 5 K for $LaCoO_{3-\delta}$ films on LSAT and STO. For reference, 1 Oe = 79.58 Am^{-1}.

R^{--} at $T = 5$ K and $H = 30$ kOe (2.4×10^6Am^{-1}, in-plane), for STO(001)/LCO($t \approx 200$ Å) and LSAT(001)/LCO($t \approx 150$ Å), respectively. Clear splitting between $R^{++}(Q)$ and $R^{--}(Q)$ is observed at this T, consistent with FM. This is highlighted in Figs. 2(b) and 2(e) by plotting the spin asymmetry, SA = $(\frac{R^{++}-R^{--}}{R^{++}+R^{--}})$. The SA is predominantly positive for films on both substrates, exhibiting clear oscillatory behavior over multiple periods. The oscillation periods are in the 0.03–0.04 Å^{-1} range, corresponding to real space lengths of 150–200 Å, immediately suggesting that FM order pervades the majority of the LCO thickness.

Quantification was achieved by refinement of the data in Figs. 4(a), 4(b), 4(d), and 4(e) using the Refl1D package [65]. To more reliably determine the depth (z) profile of the magnetic scattering length density (SLD_{mag}), unpolarized 200 K reflectometry data were also acquired (in addition to GIXR), and fit to determine the nuclear scattering length density [$SLD_{nuc}(z)$]. Only minor variation of the parameters associated with $SLD_{nuc}(z)$ (i.e., substrate and layer thicknesses and

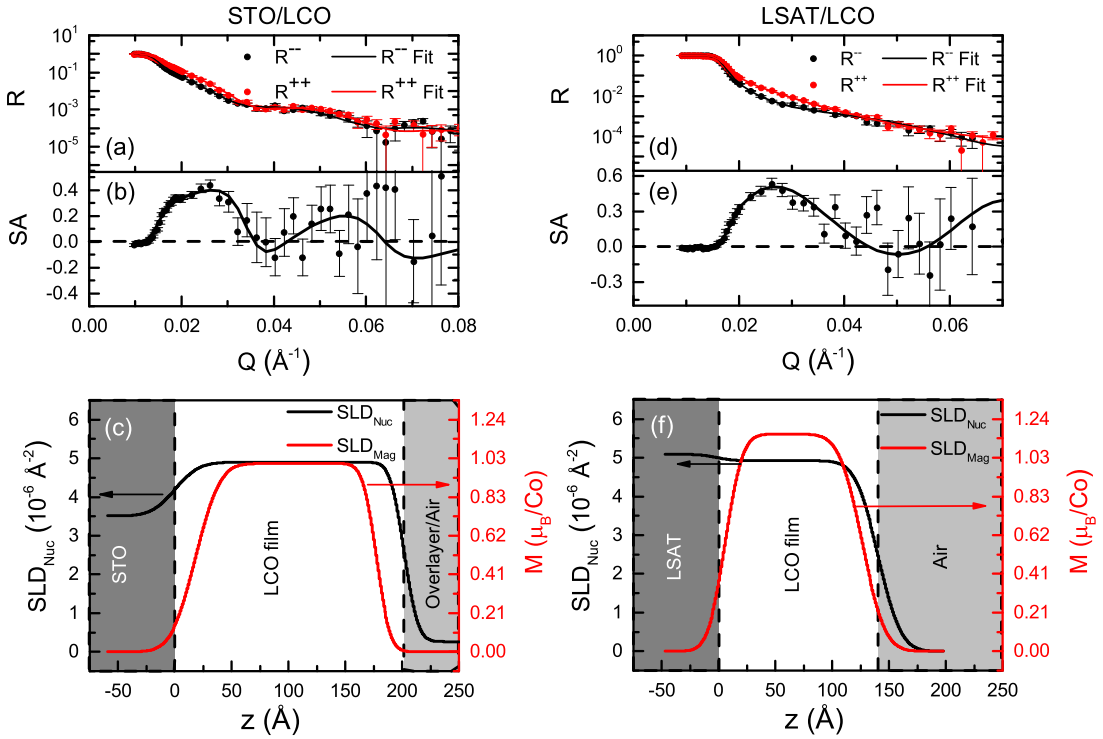

FIG. 4. Neutron reflectivity (R, top panel) and spin asymmetry (SA, bottom panel) vs scattering vector (Q) at 5 K in a 30 kOe (2.4×10^6 Am^{-1}) in-plane magnetic field for (a), (b) a 200-Å-thick $LaCoO_{3-\delta}$ film on STO, and (d), (e) a 140-Å-thick $LaCoO_{3-\delta}$ film on LSAT. In (a) and (d), black and red points are nonspin-flip R values (R^{--} and R^{++}), respectively. The solid lines are fits to the model discussed in the text, with parameters shown in Table I. (c), (f) Corresponding nuclear scattering length density (SLD_{nuc}), magnetic scattering length density (SLD_{mag}), and magnetization (M) vs depth (z). Unless otherwise noted, all uncertainties and error bars represent ±1 standard deviation.

roughnesses) was then permitted in the magnetic refinement of 5-K polarized data. Resulting fits are shown as solid lines in Figs. 4(a), 4(b), 4(d), and 4(e), with the refined $SLD_{nuc}(z)$ and $SLD_{mag}(z)$ in Figs. 4(c) and 4(f). The substrate, LCO, and region above the film are labeled and shaded in Figs. 4(c) and 4(f), the vertical dashed lines marking the nuclear (chemical) interface locations, as determined from the midpoints of the SLD_{nuc} transitions. Corresponding fit parameters [SLDs, thicknesses, roughnesses, and magnetizations (from SLD_{mag})] are given in Table I, where it can be seen that the LCO layers were split into bottom, middle, and top regions. For the STO/LCO case, a low density overlayer on the film surface was also required; such overlayers can be attributed to condensed hydrocarbons, H_2O, etc.

Considering first the nuclear (chemical) depth profile, Figs. 4(c) and 4(f) and Table I reveal fairly typical findings for epitaxial perovskite films. Top surface roughnesses of 2–4 unit cells are found (reasonable magnitudes given the large (up to 10 mm×10 mm) lateral areas probed), along with substrate/LCO interface widths of 3–4 unit cells, potentially indicating non-negligible interdiffusion. In terms of nuclear SLDs, the reflectometry data could be

TABLE I. Summary of parameters extracted from polarized neutron reflectometry (Fig. 4). Shown are the nuclear scattering length density SLD_{nuc}, thickness t, roughness σ (i.e., Gaussian interface width), and magnetization M, for each layer. These values are shown for $SrTiO_3$ (STO)/$LaCoO_3$(LCO) (top) and LSAT/LCO (bottom). As can be seen, the LCO films are split into bottom, middle, and top layers. For the STO/LCO case a low density overlayer on the LCO film surface was required to best model the data. Such overlayers can be attributed to condensed hydrocarbons, H_2O, etc. Unless otherwise noted, all uncertainties and error bars represent ±1 standard deviation.

Sample	Substrate	Bottom LCO	Middle LCO	Top LCO	Cap Layer
STO/LCO	3.51×10^{-6} Å^{-2} $t=\infty$ $\sigma=13.1$ Å ± 1.8 Å $M=0$	4.89×10^{-6} Å^{-2} $t=18.5$ Å ± 4.5 Å $\sigma=9.05$ Å ± 0.45 Å $M=0$	4.89×10^{-6} Å^{-2} $t=159.1$ Å ± 0.88 Å $\sigma=9.05$ Å ± 0.45 Å $M=1.00\,\mu_B$/Co	4.89×10^{-6} Å^{-2} $t=23.9$ Å ± 6.4 Å $\sigma=9.05$ Å ± 0.45 Å $M=0$	2.63×10^{-7} Å^{-2} $t=158$ Å ± 13 Å $\sigma=0.18$ Å ± 0.06 Å $M=0$
LSAT/LCO	5.09×10^{-6} Å^{-2} $t=\infty$ $\sigma=7.7$ Å ± 3.1 Å $M=0$	4.95×10^{-6} Å^{-2} $t=6.9$ Å ± 3.2 Å $\sigma=15.9$ Å ± 0.7 Å $M=0$	4.95×10^{-6} Å^{-2} $t=125.1$ Å ± 5.7 Å $\sigma=15.9$ Å ± 0.7 Å $M=1.14\,\mu_B$/Co	4.95×10^{-6} Å^{-2} $t=11.5$ Å ± 5.9 Å $\sigma=15.9$ Å ± 0.7 Å $M=0$	-

refined with the bulk values expected of the substrates, and with LCO values decreased only marginally from bulk (4.93×10^{-6} Å^{-2}), indicating near-single-crystal densities. Of higher interest, the refined $M(z)$ in Figs. 4(c) and 4(f), and associated parameters in Table I, reveal important findings. First, FM is confirmed to be a bulk property of these tensile strained films, with slightly higher peak M on LSAT (1.14 μ_B/Co) vs STO (1.00 μ_B/Co). [This is the same trend as seen in magnetometry in Fig. 3(b).] The magnetic thickness is nevertheless lower than the chemical thickness, magnetic dead layers being implicated at both the substrate/LCO interfaces and LCO top surfaces. These layers are approximately 2 and 4 unit cells, respectively, on LSAT, increasing to approximately 5 and 6 unit cells, respectively, on STO. We emphasize again the improved magnetic properties of LCO films on LSAT compared to STO, consistent with the slightly better structural quality. Comparisons can also be made to the recent PNR study of Guo *et al.* on STO(001)/LCO [48] where suppressed magnetization layers of thickness 4–5 unit cells were found at both the substrate/LCO and LCO/cap layer interfaces, similar to our findings. Guo *et al.* concluded reduced M in these regions, as opposed to completely dead layers, but from data taken to larger maximum Q, and thus with higher resolution. In summary, the PNR data and analysis presented here confirm bulk long-range FM in LCO films on both LSAT and STO, albeit with improved magnetization depth profile (i.e., lower dead layer thickness) on LSAT.

C. Electronic transport

Motivated by the situation summarized in the Introduction, detailed transport and magnetotransport measurements were also made. Shown in Fig. 5(a) is the zero-field $\rho(T)$ ($\log_{10}\rho$ scale) of representative 130-Å-thick LCO films on SLAO, LAO, LSAT, and STO substrates. These data are plotted from 400 K to the lowest T that could be measured (75–100 K depending on the specific resistance) and are compared in Fig. 5(a) to a data set on a bulk polycrystalline sample, selected for its extended T range [20]. Semiconducting behavior is seen in all films, but, interestingly, with approximately 0.1 to 1 Ωcm resistivity at 300 K, i.e., lower ρ than bulk, regardless of the sign of the strain. Such 300-K resistivities are at the lower end of the reported range for epitaxial LCO [37,42,62], although the literature is sparse. Notably, $\rho(T)$ is similar under compressive and tensile strain (with the exception of somewhat lower ρ under compression), despite the strikingly different magnetic properties. As an aside, the lowest T at which transport measurements could be made under compression was 75 K (on LSAT), only marginally below T_C, meaning that magnetotransport studies in the FM state of epitaxial LCO films remain a challenge.

Figure 5(b) plots the same data as $\log_{10}\rho$vs T^{-1}, exposing Arrhenius behavior between about 250 K and the lowest T. The extracted activation energy E_a varies between 53 and 103 meV, being generally lower under compression than under tension. Consistent with the lower overall ρ, these energies are also lower than those obtained in the same T range in bulk [143 meV, see Fig. 5(b)]. Within a simple semiconductor physics interpretation this 143 meV bulk energy could indicate intrinsic conduction across a roughly 0.3 eV gap (not out

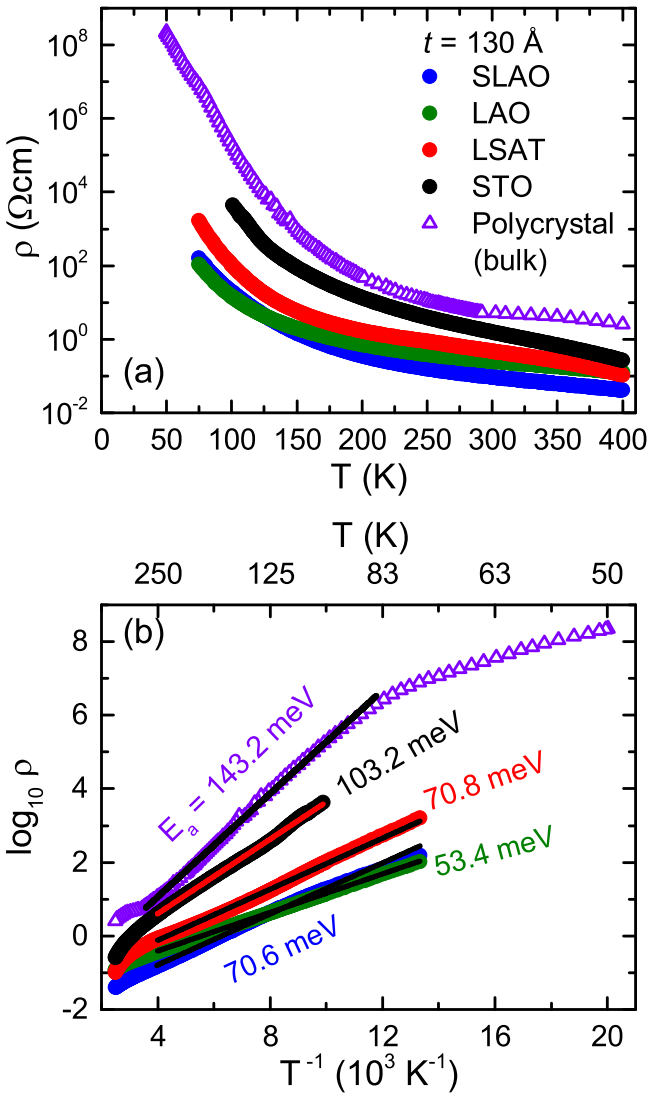

FIG. 5. (a) Temperature (T) dependence of zero magnetic field resistivity (ρ, on a $\log_{10}$ scale) for 130-Å-thick $LaCoO_{3-\delta}$ films on various substrates. (b) Corresponding $\log_{10}(\rho)$ vs $1/T$ plot, along with low T straight-line fits yielding the activation energies shown. Bulk polycrystalline data are shown for comparison [20].

of the question for LCO [18]), or a Fermi level 150–300 meV from the conduction or valence band edge, dependent on compensation and doping. The lower E_a in films could then indicate higher doping levels; this possibility was thus probed via Hall measurements.

Figures 6(a) and 6(b) show 225 K transverse (Hall) resistivity ρ_{xy} vs H for representative 130-Å-thick LCO films on SLAO and LAO [compressive strain, Fig. 6(a)] and LSAT and STO [tensile strain, Fig. 6(b)], revealing a major finding of this work. Specifically, a simple H-linear Hall signal is found in both cases, with relatively large magnitudes of the Hall coefficient (R_H), *but opposite signs under compression* [Fig. 6(a)] *and tension* [Fig. 6(b)]. The sign under compressive strain is holelike (positive R_H), as in nominally undoped bulk crystals [18], while the sign under tension is electronlike (negative R_H). The magnitudes of the Hall coefficient also vary by an order-of-magnitude, tensile-strained LCO films

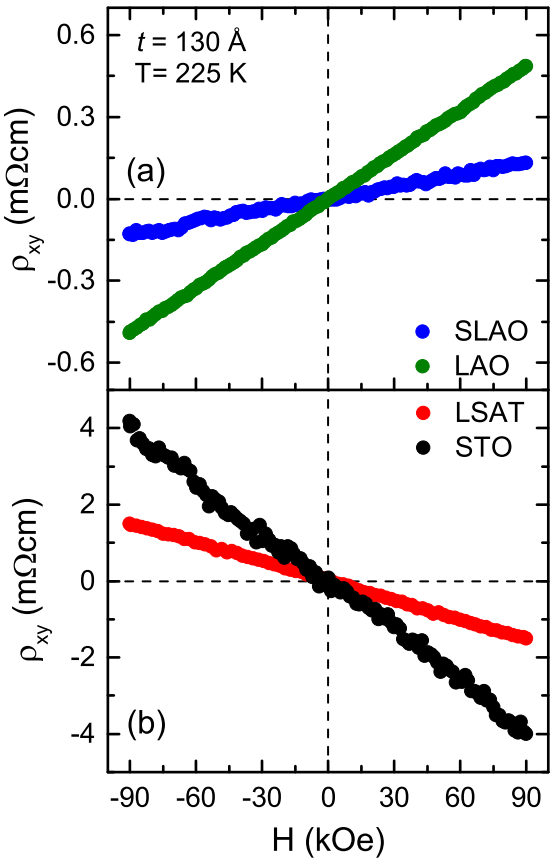

FIG. 6. Magnetic field (H) dependence of the 225 K Hall resistivity (ρ_{xy}) of 130-Å-thick $LaCoO_{3-\delta}$ films under (a) compressive strain on SLAO and LAO, and (b) tensile strain on LSAT and STO. As is typical, a zero field background has been subtracted.

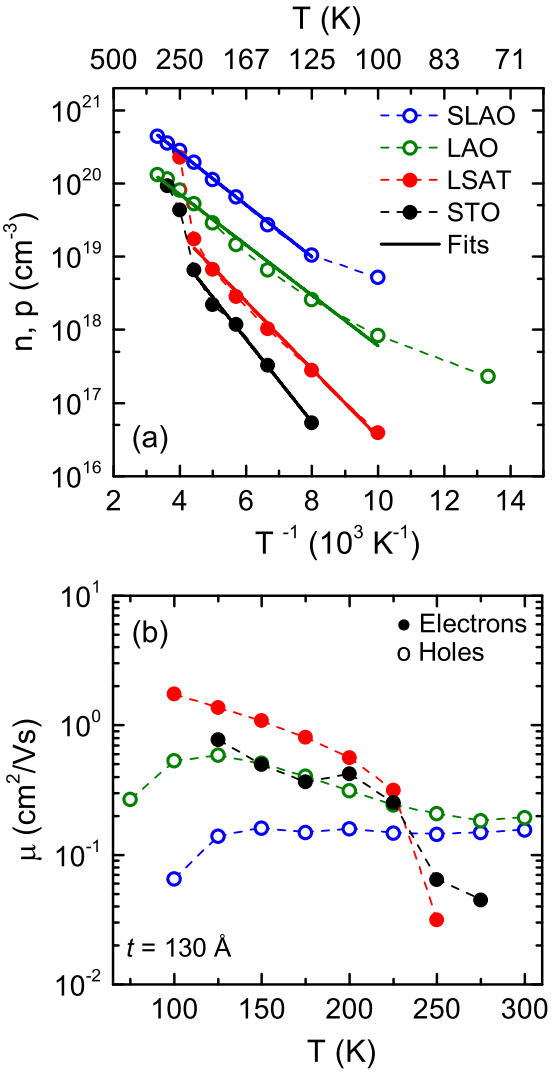

FIG. 7. (a) Hall electron or hole density ($\log_{10}$ scale, solid symbols for electrons, open symbols for holes) vs inverse temperature (T) for 130-Å-thick $LaCoO_{3-\delta}$ films on various substrates. Solid lines are straight line (Arrhenius) fits. (b) Corresponding Hall mobility (μ, $\log_{10}$ scale) vs T.

having larger R_H than compressive films. Given the simple linear behavior in $\rho_{xy}(H)$ to 90 kOe (7.2×10^6 Am^{-1}), which is true at all T, there is no indication of multiple carrier types involved in the transport. In Fig. 7(a) we thus plot the apparent electron or hole density ($1/|R_H|e$) vs T^{-1}, using solid symbols for electronlike and open symbols for holelike. Data are shown for the same films as in Figs. 5 and 6 (on SLAO, LAO, LSAT, and STO), the solid lines being straight-line (Arrhenius) fits. The inversion from holelike to electronlike R_H under tensile strain is seen to be robust over the entire T range, the 225 K Hall electron densities under tension being in the mid 10^{18}–10^{19} cm^{-3} range, compared to hole densities under compression of mid 10^{19}–10^{20} cm^{-3}. Simple activated behavior (solid lines) is also seen over the majority of the probed T range, in agreement with $\rho(T)$ in Fig. 5(b). Quantitatively, E_a values from the Hall carrier densities in Fig. 7(a) are 73, 70, 95, and 116 meV on SLAO, LAO, LSAT, and STO, respectively, agreeing well with the 71, 53, 71, and 103 meV from resistivity in Fig. 5(b). At the highest T, the tensile-strained LCO films show a possible break in slope to higher E_a (100′s of meV), i.e., similar values to bulk [20]. At the lowest T, films under compression only show a potential break to lower E_a. This would be consistent with the behavior seen across the spin-state transition in bulk [20], but could not be probed to sufficiently low T to confirm this.

Combining these Hall electron or hole densities with $\rho(T)$ provides the apparent Hall mobility, $\mu(T)$, which is plotted in Fig. 7(b) for the same films. μ typically increases on cooling from 300 to down to ∼100 K. Under compressive strain the peak hole mobility reaches 0.6 cm^2 V^{-1} s^{-1}, the high T values approaching 0.1–0.2 cm^2 V^{-1} s^{-1}, almost an order-of-magnitude larger than the apparent bulk single crystal hole mobility of 0.03 cm^2 V^{-1} s^{-1} at 340 K [18]. Under tensile strain the peak carrier (electron) mobility is yet larger, reaching almost 2 cm^2 V^{-1} s^{-1} at 100 K on LSAT. Figures 7(a) and 7(b) thus illustrate that the generally lower resistivities in compressive LCO films [see Fig. 5(a)] are due to higher carrier density [Fig. 7(a)], despite typically lower mobility [Fig. 7(b)].

Taken at face value, the data of Figs. 6 and 7 indicate an unanticipated inversion in majority carrier type, from holes (i.e., p-type behavior) in compressive LCO films (as in bulk), to electrons (i.e., n-type) under tension. Caution is warranted,

however, as some transport mechanisms are known to suppress, and even invert, the sign of R_H, in the absence of a true inversion in majority carrier type [73–76]. Hopping transport, particularly variable-range hopping [77,78], is a prime example [73–76]. A key observation in this regard is the simple activated behavior displayed by $\rho(T)$ [Fig. 5(b)] and $1/e|R_H(T)|$ [Fig. 7(a)], which is inconsistent with variable range hopping [78]. The maximum μ in these LCO films also reaches $2\,\mathrm{cm^2\,V^{-1}\,s^{-1}}$ [Fig. 7(b)], which, while modest, safely exceeds the mobilities at which hopping-induced inversions of R_H typically occur (often $\sim 0.1\,\mathrm{cm^2\,V^{-1}\,s^{-1}}$) [76]. The mobility also increases on cooling over the majority of the T range in Fig. 7(b), indicating phonon-limited diffusive transport as opposed to hopping. Finally, the E_a values here are also much larger than typical for nearest neighbor hopping [77,78]. Based on these observations, an artificial sign inversion of R_H due to variable range or nearest neighbor hopping transport is unlikely. Hopping of polarons is another possibility that should be considered, as the Hall effect in polaronic conduction is also complex, and need not reflect the true sign of the charge carriers [79]. While the T dependence of the resistivity and apparent carrier density observed here do not explicitly rule out polaron hopping, it is shown below that a compelling, self-consistent explanation for the transport phenomena we observe can be obtained from a band transport model. We note that the highest mobilities observed here also occur under tension, when R_H is inverted, another argument against the inversion being caused by an artifact of any form of hopping conduction. A second possible artifact is provided by the anomalous Hall effect, which could be anticipated in tensile-strained films as FM emerges. A negative anomalous Hall coefficient combined with a large magnetic susceptibility could potentially overwhelm an underlying positive ordinary Hall coefficient, leading to apparent inversion of R_H. The anomalous Hall coefficient in Sr-doped LCO is positive in both bulk and film form, however [63,80,81], $\rho_{xy}(H)$ in tensile-strained LCO films exhibits no sign of nonlinearity, and $R_H(T)$ is inconsistent with a Curie-Weiss T dependence of the susceptibility. This possibility is thus also ruled out. We, therefore, interpret the inversion of R_H shown in Figs. 6 and 7 as a true inversion of the majority carrier type, from holes under compression, to electrons under tension. Remarkably, while thus far overlooked, there is thus a direct correlation in LCO films between the existence of long-range FM and n-type transport, both of which occur only under tensile strain.

In summary, a number of unanticipated observations result from simple transport analyses. Comparing bulk and thin film LCO, lower ρ, lower E_a, and higher μ are found in epitaxial films. Comparing tensile and compressive strain, lower carrier density and higher μ occur in films under tension, along with a striking inversion of the majority carrier type from holes to electrons. We show below that strain-dependent DFT-based band structure calculations, combined with straightforward arguments regarding orbital energies and occupations, provide simple qualitative explanations for these phenomena.

D. Electronic structure calculations

DFT+U calculations of electronic structure were performed as a function of biaxial strain (from -3% to $+3\%$) by constraining the in-plane LCO lattice parameters, and then subsequently relaxing the structure. As discussed in further detail in Supplemental Material Section A (Figs. S1, S2, S3 and Table S1) [82], and as is often the case in perovskite oxides, the calculated ground state octahedral tilt pattern varies with strain. The predicted tilt pattern (in Glazer notation [83]) at the largest negative (i.e., compressive) strains is $a^0a^0c^-$ (associated with the $I4/mcm$ space group), transforming at approximately -1.75% to $a^-a^-c^-$ ($C2/c$ space group), then to $a^-a^-c^+$ ($Pnma$ space group) at all strains above $\sim 0.75\%$ (i.e., more tensile). At zero strain the predicted ground state tilt pattern is thus $a^-a^-c^-$ ($C2/c$), not the bulk $a^-a^-a^-$ ($R\bar{3}c$), due to the constrained in-plane lattice vectors; without such constraints the predicted structure indeed becomes $R\bar{3}c$. These DFT-based structural predictions were directly tested via SXRD measurements of the half-order Bragg peaks that arise from unit cell doubling due to CoO_6 octahedral rotations [84]. As discussed in Supplemental Material Section B (Fig. S4 [82]), measurements of intensities and systematic absences of these peaks provide not only the tilt pattern, but also the CoO_6 octahedral rotation angles [84]. Such experiments were done on films on SLAO (-1.42% strain) and STO ($+2.49\%$ strain), at 300 K, establishing the $a^-a^-c^-$ tilt pattern ($C2/c$ space group), in *both* cases. This is in agreement with DFT under -1.42% strain (SLAO), but at apparent odds with it under $+2.49\%$ strain (STO). The SXRD measurements were performed at 300 K, however, and $T = 0$ DFT puts the experimentally observed structure at $+2.49\%$ strain as little as 3.1 meV/formula unit above the ground state, providing a simple potential explanation for this apparent disagreement (see Supplemental Material Section A, Fig. S2 for further details [82]).

Based on these predicted ground-state structures, band structure calculations were performed vs strain. Figures 8(a) and 8(b) show representative examples at -1.5% strain [compressive, Fig. 8(a)] and $+2.5\%$ strain [tensile, Fig. 8(b)], corresponding to LCO films on SLAO and STO substrates, i.e., the full span of heteroepitaxial strain studied experimentally. At this level of theory, LCO is indeed nonmetallic, the (direct) semiconducting energy gaps in Figs. 8(a) and 8(b) being 0.44 and 0.46 eV, respectively. As expected (see Supplemental Material Section A [82] for more details), this gap is dictated by the separation between the Co e_g states that form the conduction band minimum and the hybridized Co t_{2g}−O $2p$ states at the valence band maximum; the localized La $4f$ states are at much higher energy. Most significantly, especially for comparison with transport data, the detailed features of the band structure at the valence band maximum, and particularly the conduction band minimum, are strongly strain-dependent. At the valence band maximum, for example, Figs. 8(a) and 8(b) show a substantial decrease in dispersion near the Γ point on going from compressive to tensile strain. This occurs because the most dispersive t_{2g} band narrows, and shifts below other t_{2g} bands, likely due to hopping amplitude changes induced by Co–O–Co bond angle shifts. Regardless of exact origin, this would be expected to increase the hole effective mass (m_h^*) under tension. At the same time, the states that dominate the conduction band minimum become distinctly more dispersive under tension compared to compression [compare Figs. 8(a) and 8(b)],

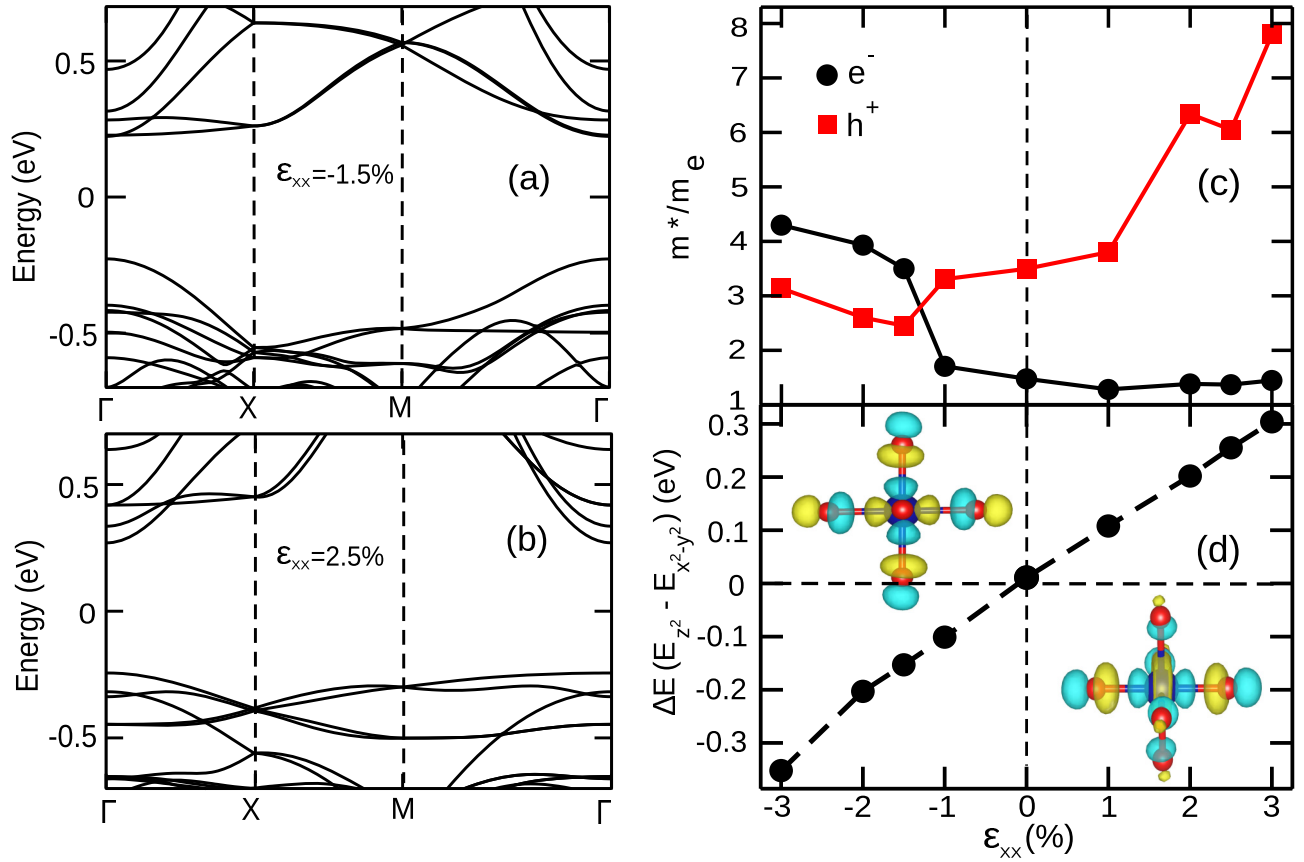

FIG. 8. Density functional theory electronic band structure for $LaCoO_3$ films under (a) 1.5% compressive strain and (b) 2.5% tensile strain. (c) Electron and hole (black and red symbols) effective masses (m^*/m_e, where m_e is the free electron mass, computed along the Γ-X direction) vs in-plane strain (ε_{xx}). (d) Energy Splitting between the cobalt e_g-like Wannier orbitals ($\Delta E = E_{z^2} - E_{x^2-y^2}$) vs biaxial strain ($\varepsilon_{xx}$). The two insets show the $d_{x^2-y^2}$ (top left) and d_{z^2} (bottom right) Wannier orbitals.

which would be expected to lead to a decrease in electron effective mass (m_e^*) under tension. This occurs because under tensile strain the $d_{x^2-y^2}$ orbital, which gives rise to bands that are dispersive in the film plane, becomes lower in energy than the d_{z^2} one, the opposite occurring under compression. This is illustrated in Fig. 8(d), where Wannier function calculations are used to extract the energy difference between d_{z^2} and $d_{x^2-y^2}$ orbitals vs strain. We note that this is in good general agreement with the recent x-ray linear dichroism results of Guo *et al.*, where high $d_{x^2-y^2}$ orbital polarization was deduced under tensile strain [47].

Quantification of these strain-induced band structure changes was achieved by fitting the low energy (within 0.12 eV) regions near the conduction band minimum and valence band maximum to $E = \hbar^2 k^2 / 2 m_e^* m_e$ and $E = \hbar^2 k^2 / 2 m_h^* m_e$, respectively ($m_e$ is the bare electron mass). Effective masses were thus determined along the Γ-X [where $X = (0.5, 0, 0)\pi / a_{pc}$] and Γ-M [where $M = (0.5, 0.5, 0)\pi / a_{pc}$] directions, as shown in Figs. 8(a) and 8(b). The results for the Γ-X direction are plotted as a function of strain in Fig. 8(c), revealing a striking strain-driven crossover in the relative effective masses of holes and electrons; results for the Γ-M direction (not shown) reveal a similar trend. In Fig. 8(c), m_h^* is seen to approximately double from -1.5% to $+2.5\%$ strain, while m_e^* decreases by around a factor of 4. The ratio m_e^*/m_h^* thus falls by almost an order of magnitude from -1.5% (compressive) to 2.5% (tensile) strain. Note that this trend was also checked in the $a^-a^-c^-$ case, found in experiment under both tension and compression; very similar effective mass values were found.

IV. DISCUSSION

We propose that these electronic structure calculations, in combination with straightforward inferences supported by prior literature, provide explanations for several of the transport phenomena presented here, in particular the majority carrier inversion. The first important point in this regard is that the data of Fig. 8(c) establish substantially lower effective mass at the e_g-derived conduction band minimum than the t_{2g}-derived valence band maximum for tensile films. Comparing -1.5% and $+2.5\%$ strain, equivalent to SLAO and STO substrates, m_e^*/m_h^* in fact decreases from ~1.4 to ~0.2. For comparable scattering rates for electrons and holes this strong asymmetry in effective mass will increase electron mobility over hole mobility, as clearly supported by the data of Fig. 7(b). A second important point, well supported by the literature on LCO films [32,36,39–41,43–47,49–51], is that FM under tensile strain must reflect suppression of the bulk spin-state transition and stabilization of a nonzero spin state. Regardless of the details

of the tensile-strain-stabilized nonzero spin state (be it uniform or a spin-state superstructure), this necessarily involves a tensile-strain-driven redistribution of orbital occupancies from t_{2g} to e_g. The e_g-derived conduction band minimum will thus populate with electrons, the lower effective mass and higher mobility for electrons leading to inversion of the Hall coefficient and majority carrier type, providing a simple explanation for a central result of this work.

V_O-driven *n*-type doping is also a possibility in LCO. There are, however, clear indications that this cannot explain a crossover from *p*-type under compression to *n*-type under tension. First, while quantification is difficult, and is not attempted here, the STEM images in Figs. 2(c) and 2(d) clearly indicate V_O order, and thus substantial V_O densities, in both tensile-strained *and* compressive-strained films. There is thus no clear reason to expect much heavier V_O doping under tension vs compression, and this is indeed not supported by the lattice parameter trends [see Fig. 2(a)]. As additional support for this we note that calculated V_O formation enthalpies in lightly Sr-doped LCO films are similar under compressive and tensile strain, differing by less than 0.1 eV at $\pm 1\%$ strain [85]. There is thus no expected thermodynamic driving force for V_O formation under tension vs compression, certainly not at the level required to generate the difference in carrier density shown for tensile and compressive films in Fig. 7(a).

V. SUMMARY

A comprehensive study of structural, magnetic, and electronic transport properties of epitaxial LCO films (100 to 220-Å-thick) has been presented, imposing heteroepitaxial strains between -1.4% (compressive) and $+2.5\%$ (tensile). Thorough characterization of the structure and morphology with SXRD, STEM/EELS, AFM, and GIXR, reveals high-quality, smooth epitaxial films that exhibit superstructures associated with V_O order and periodic lateral ferroelastic twin domains. FM occurs only under tensile strain, with T_C up to 83 K and M_s up to 1.1 μ_B/Co. PNR measurements confirm that this FM is a bulk property, although unit-cell-level interfacial dead layers do form. Semiconducting transport occurs regardless of the sign of the strain, similar to bulk, albeit with lower resistivity and activation energy. Most importantly, a striking inversion of the majority carrier type occurs under tensile strain, from the *p*-type seen in bulk and under compression, to *n*-type under tension. This inversion is accompanied by a significant increase in mobility for tensile vs compressive films. These results are interpreted in terms of a tensile-strain-induced redistribution of orbital occupancies towards e_g states, in concert with substantial lowering of the electron effective mass, as deduced from DFT-based calculations. These results provide further understanding of the FM state in strained epitaxial LCO, in particular a previously undetected link between magnetism and transport.

ACKNOWLEDGMENTS

This work was supported primarily by the U.S. Department of Energy (DOE) through the University of Minnesota (UMN) Center for Quantum Materials under Grant No. DE-SC-0016371. Computational work by A.P. was supported by the National Science Foundation through the UMN MRSEC under Award No. DMR-1420013. Parts of this work were performed in the Characterization Facility, UMN, which receives partial support from the National Science Foundation (NSF) through the MSREC. Part of this work also used resources of the Advanced Photon Source, a DOE Office of Science user facility operated by Argonne National Laboratory under Grant No. DE-AC02-06CH11357. We gratefully acknowledge J. Borchers for useful discussions. Certain commercial equipment, instruments, or materials are identified in this paper to foster understanding. Such identification does not imply recommendation or endorsement by the National Institute of Standards and Technology, nor does it imply that the materials or equipment identified are necessarily the best available for the purpose.

[1] R. Ramesh and D. G. Schlom, MRS Bull. **33**, 1006 (2008).
[2] J. Chakhalian, A. J. Millis, and J. Rondinelli, Nat. Mater. **11**, 92 (2012).
[3] J. H. Ngai, F. J. Walker, and C. H. Ahn, Annu. Rev. Mater. Res. **44**, 1 (2014).
[4] H. Y. Hwang, Y. Iwasa, M. Kawasaki, B. Keimer, N. Nagaosa, and Y. Tokura, Nat. Mater. **11**, 103 (2012).
[5] J. H. Haeni, P. Irvin, W. Chang, R. Uecker, P. Reiche, Y. L. Li, S. Choudhury, W. Tian, M. E. Hawley, B. Craigo, A. K. Tagantsev, X. Q. Pan, S. K. Streiffer, L. Q. Chen, S. W. Kirchoefer, J. Levy, and D. G. Schlom, Nature (London) **430**, 758 (2004).
[6] D. G. Schlom, L.-Q. Chen, C.-B. Eom, K. M. Rabe, S. K. Streiffer, and J.-M. Triscone, Annu. Rev. Mater. Res. **37**, 589 (2007).
[7] J. H. Lee, L. Fang, E. Vlahos, X. Ke, Y. W. Jung, L. F. Kourkoutis, J.-W. Kim, P. J. Ryan, T. Heeg, M. Roeckerath, V. Goian, M. Bernhagen, R. Uecker, P. C. Hammel, K. M. Rabe, S. Kamba, J. Schubert, J. W. Freeland, D. A. Muller, C. J. Fennie, P. Schiffer, V. Gopalan, E. Johnston-Halperin, and D. G. Schlom, Nature (London) **466**, 954 (2010).
[8] A. Bhattacharya and S. J. May, Annu. Rev. Mater. Res. **44**, 65 (2014).
[9] D. Fuchs, C. Pinta, T. Schwarz, P. Schweiss, P. Nagel, S. Schuppler, R. Schneider, M. Merz, G. Roth, and H. v. Löhneysen, Phys. Rev. B **75**, 144402 (2007).
[10] P. M. Raccah and J. B. Goodenough, Phys. Rev. **155**, 932 (1967).
[11] P. G. Radaelli and S. W. Cheong, Phys. Rev. B **66**, 094408 (2002).
[12] K. Asai, P. Gehring, H. Chou, and G. Shirane, Phys. Rev. B **40**, 10982 (1989).
[13] K. Asai, O. Yokokura, N. Nishimori, H. Chou, J. M. Tranquada, G. Shirane, S. Higuchi, Y. Okajima, and K. Kohn, Phys. Rev. B **50**, 3025 (1994).
[14] M. A. Korotin, S. Y. Ezhov, I. V. Solovyev, V. I. Anisimov, D. I. Khomskii, and G. A. Sawatzky, Phys. Rev. B **54**, 5309 (1996).
[15] S. Yamaguchi, Y. Okimoto, H. Taniguchi, and Y. Tokura, Phys. Rev. B **53**, R2926 (1996).
[16] S. Yamaguchi, Y. Okimoto, and Y. Tokura, Phys. Rev. B **55**, R8666 (1997).

[17] M. Imada, A. Fujimori, and Y. Tokura, Rev. Mod. Phys. **70**, 1039 (1998).

[18] Y. Tokura, Y. Okimoto, S. Yamaguchi, H. Taniguchi, T. Kimura, and H. Takagi, Phys. Rev. B **58**, R1699 (1998).

[19] C. Zobel, M. Kriener, D. Bruns, J. Baier, M. Grüninger, T. Lorenz, P. Reutler, and A. Revcolevschi, Phys. Rev. B **66**, 020402(R) (2002).

[20] S. R. English, J. Wu, and C. Leighton, Phys. Rev. B **65**, 220407(R) (2002).

[21] Z. Ropka and R. J. Radwanski, Phys. Rev. B **67**, 172401 (2003).

[22] R. J. Radwanski and Z. Ropka, Phys. B **359-361**, 1354 (2005).

[23] A. Podlesnyak, S. Streule, J. Mesot, M. Medarde, E. Pomjakushina, K. Conder, A. Tanaka, M. W. Haverkort, and D. I. Khomskii, Phys. Rev. Lett. **97**, 247208 (2006).

[24] M. W. Haverkort, Z. Hu, J. C. Cezar, T. Burnus, H. Hartmann, M. Reuther, C. Zobel, T. Lorenz, A. Tanaka, N. B. Brookes, H. H. Hsieh, H.-J. Lin, C. T. Chen, and L. H. Tjeng, Phys. Rev. Lett. **97**, 176405 (2006).

[25] R. F. Klie, J. C. Zheng, Y. Zhu, M. Varela, J. Wu, and C. Leighton, Phys. Rev. Lett. **99**, 047203 (2007).

[26] Y. Lee and B. N. Harmon, J. Appl. Phys. **113**, 17E145 (2013).

[27] B. Chakrabarti, T. Birol, and K. Haule, Phys. Rev. Mater. **1**, 064403 (2017).

[28] E. L. Nagaev and A. I. Podel'shchikov, J. Phys.: Condens. Matter **8**, 5611 (1996).

[29] J.-Q. Yan, J.-S. Zhou, and J. B. Goodenough, Phys. Rev. B **70**, 014402 (2004).

[30] S. R. Giblin, I. Terry, S. J. Clark, T. Prokscha, D. Prabhakaran, A. T. Boothroyd, J. Wu, and C. Leighton, Europhys. Lett. **70**, 677 (2005).

[31] S. R. Giblin, I. Terry, D. Prabhakaran, A. T. Boothroyd, and C. Leighton, Phys. Rev. B **79**, 174410 (2009).

[32] N. Biškup, J. Salafranca, V. Mehta, M. P. Oxley, Y. Suzuki, S. J. Pennycook, S. T. Pantelides, and M. Varela, Phys. Rev. Lett. **112**, 087202 (2014).

[33] S. El-Khatib, D. Phelan, J. G. Barker, H. Zheng, J. F. Mitchell, and C. Leighton, Phys. Rev. B **92**, 060404(R) (2015).

[34] A. M. Durand, D. P. Belanger, T. J. Hamil, F. Ye, S. Chi, J. A. Fernandez-Baca, C. H. Booth, Y. Abdollahian, and M. Bhat, J. Phys.: Condens. Matter **27**, 176003 (2015).

[35] D. Fuchs, E. Arac, C. Pinta, S. Schuppler, R. Schneider, and H. v. Löhneysen, Phys. Rev. B **77**, 014434 (2008).

[36] V. V. Mehta, N. Biskup, C. Jenkins, E. Arenholz, M. Varela, and Y. Suzuki, Phys. Rev. B **91**, 144418 (2015).

[37] J. W. Freeland, J. X. Ma, and J. Shi, Appl. Phys. Lett. **93**, 212501 (2008).

[38] S. Park, P. Ryan, E. Karapetrova, J. W. Kim, J. X. Ma, J. Shi, J. W. Freeland, and W. Wu, Appl. Phys. Lett. **95**, 072508 (2009).

[39] G. E. Sterbinsky, P. J. Ryan, J.-W. Kim, E. Karapetrova, J. X. Ma, J. Shi, and J. C. Woicik, Phys. Rev. B **85**, 020403(R) (2012).

[40] W. S. Choi, J.-H. Kwon, H. Jeen, J. E. Hamann-Borrero, A. Radi, S. Macke, R. Sutarto, F. He, G. A. Sawatzky, V. Hinkov, M. Kim, and H. N. Lee, Nano Lett. **12**, 4966 (2012).

[41] J. Fujioka, Y. Yamasaki, H. Nakao, R. Kumai, Y. Murakami, M. Nakamura, M. Kawasaki, and Y. Tokura, Phys. Rev. Lett. **111**, 027206 (2013).

[42] F. Rivadulla, Z. Bi, E. Bauer, B. Rivas-Murias, J. M. Vila-Fungueiriño, and Q. Jia, Chem. Mater. **25**, 55 (2013).

[43] J.-H. Kwon, W. S. Choi, Y.-K. Kwon, R. Jung, J.-M. Zuo, H. N. Lee, and M. Kim, Chem. Mater. **26**, 2496 (2014).

[44] J. Fujioka, Y. Yamasaki, A. Doi, H. Nakao, R. Kumai, Y. Murakami, M. Nakamura, M. Kawasaki, T. Arima, and Y. Tokura, Phys. Rev. B **92**, 195115 (2015).

[45] G. E. Sterbinsky, R. Nanguneri, J. X. Ma, J. Shi, E. Karapetrova, J. C. Woicik, H. Park, J.-W. Kim, and P. J. Ryan, Phys. Rev. Lett. **120**, 197201 (2018).

[46] Y. Yokoyama, Y. Yamasaki, M. Taguchi, Y. Hirata, K. Takubo, J. Miyawaki, Y. Harada, D. Asakura, J. Fujioka, M. Nakamura, H. Daimon, M. Kawasaki, Y. Tokura, and H. Wadati, Phys. Rev. Lett. **120**, 206402 (2018).

[47] E.-J. Guo, R. D. Desautels, D. Keavney, A. Herklotz, T. Z. Ward, M. R. Fitzsimmons, and H. N. Lee, Phys. Rev. Mater. **3**, 014407 (2019).

[48] E.-J. Guo, R. Desautels, D. Lee, M. A. Roldan, Z. Liao, T. Charlton, H. Ambaye, J. Molaison, R. Boehler, D. Keavney, A. Herklotz, T. Z. Ward, H. N. Lee, and M. R. Fitzsimmons, Phys. Rev. Lett. **122**, 187202 (2019).

[49] E.-J. Guo, R. Desautels, D. Keavney, M. A. Roldan, B. J. Kirby, D. Lee, Z. Liao, T. Charlton, A. Herklotz, T. Zac Ward, M. R. Fitzsimmons, and H. N. Lee, Sci. Adv. **5**, eaav5050 (2019).

[50] C. Pinta, D. Fuchs, M. Merz, M. Wissinger, E. Arac, H. v. Löhneysen, A. Samartsev, P. Nagel, and S. Schuppler, Phys. Rev. B **78**, 174402 (2008).

[51] M. Merz, P. Nagel, C. Pinta, A. Samartsev, H. v. Löhneysen, M. Wissinger, S. Uebe, A. Assmann, D. Fuchs, and S. Schuppler, Phys. Rev. B **82**, 174416 (2010).

[52] D. Fuchs, L. Dieterle, E. Arac, R. Eder, P. Adelmann, V. Eyert, T. Kopp, R. Schneider, D. Gerthsen, and H. v. Löhneysen, Phys. Rev. B **79**, 024424 (2009).

[53] U. Gebhardt, N. V. Kasper, A. Vigliante, P. Wochner, H. Dosch, F. S. Razavi, and H.-U. Habermeier, Phys. Rev. Lett. **98**, 096101 (2007).

[54] M. A. Torija, M. Sharma, J. Gazquez, M. Varela, C. He, J. Schmitt, J. A. Borchers, M. Laver, S. El-Khatib, and C. Leighton, Adv. Mater. **23**, 2711 (2011).

[55] J. Gazquez, S. Bose, M. Sharma, M. A. Torija, S. J. Pennycook, C. Leighton, and M. Varela, APL Mater. **1**, 012105 (2013).

[56] D. O. Klenov, W. Donner, B. Foran, and S. Stemmer, Appl. Phys. Lett. **82**, 3427 (2003).

[57] H. Seo, A. Posadas, and A. A. Demkov, Phys. Rev. B **86**, 014430 (2012).

[58] J. Wu and C. Leighton, Phys. Rev. B **67**, 174408 (2003).

[59] J. M. Rondinelli and N. A. Spaldin, Phys. Rev. B **79**, 054409 (2009).

[60] K. Gupta and P. Mahadevan, Phys. Rev. B **79**, 020406(R) (2009).

[61] H. Hsu, P. Blaha, and R. M. Wentzcovitch, Phys. Rev. B **85**, 140404(R) (2012).

[62] B. Liu, Y. Wang, G. Liu, H. Feng, H. Yang, and J. Sun, J. Appl. Phys. **120**, 154103 (2016).

[63] J. Walter, H. Wang, B. Luo, C. D. Frisbie, and C. Leighton, ACS Nano **10**, 7799 (2016).

[64] S. Xu, Y. Moritomo, K. Mori, T. Kamiyama, T. Saitoh, and A. Nakamura, J. Phys. Soc. Jpn. **70**, 3296 (2001).

[65] B. J. Kirby, P. A. Kienzle, B. B. Maranville, N. F. Berk, J. Krycka, F. Heinrich, and C. F. Majkrzak, Curr. Opin. Colloid Interface Sci. **17**, 44 (2012).
[66] G. Kresse and D. Joubert, Phys. Rev. B **59**, 1758 (1999).
[67] J. P. Perdew, A. Ruzsinszky, G. I. Csonka, O. A. Vydrov, G. E. Scuseria, L. A. Constantin, X. Zhou, and K. Burke, Phys. Rev. Lett. **100**, 136406 (2008).
[68] S. L. Dudarev, G. A. Botton, S. Y. Savrasov, C. J. Humphreys, and A. P. Sutton, Phys. Rev. B **57**, 1505 (1998).
[69] A. A. Mostofi, J. R. Yates, Y.-S. Lee, I. Souza, D. Vanderbilt, and N. Marzari, Comput. Phys. Commun. **178**, 685 (2008).
[70] N. Marzari, A. A. Mostofi, J. R. Yates, I. Souza, and D. Vanderbilt, Rev. Mod. Phys. **84**, 1419 (2012).
[71] C. J. Howard, B. J. Kennedy, and B. C. Chakoumakos, J. Phys.: Condens. Matter **12**, 349 (2000).
[72] J. Walter, G. Yu, B. Yu, A. Grutter, B. Kirby, J. Borchers, Z. Zhang, H. Zhou, T. Birol, M. Greven, and C. Leighton, Phys. Rev. Mater. **1**, 071403(R) (2017).
[73] P. G. Le Comber, D. I. Jones, and W. E. Spear, Philos. Mag. **35**, 1173 (1977).
[74] Yu. M. Gal'perin, E. P. German, and V. G. Karpov, Zh. Eksp. Teor. Fiz. **99**, 343 (1991) [Sov. Phys. JETP **72**, 193 (1991)].
[75] L. Friedman, J. Non-Cryst. Solids **6**, 329 (1971).
[76] X. Zhang, M. Li, J. Walter, L. O'Brien, M. A. Manno, B. Voigt, F. Mork, S. V. Baryshev, J. Kakalios, E. S. Aydil, and C. Leighton, Phys. Rev. Mater. **1**, 015402 (2017).
[77] N. F. Mott, *Metal Insulator Transitions*, 2nd ed. (Taylor and Francis, London, 1990).
[78] B. I. Shklovskii and A. L. Efros, *Electronic Properties of Doped Semiconductors* (Springer, Berlin, 1984).
[79] D. Emin, *Polarons* (Cambridge University Press, Cambridge, 2013).
[80] Y. Onose and Y. Tokura, Phys. Rev. B **73**, 174421 (2006).
[81] C. He, S. Eisenberg, C. Jan, H. Zheng, J. F. Mitchell, and C. Leighton, Phys. Rev. B **80**, 214411 (2009).
[82] See Supplemental Material at http://link.aps.org/supplemental/10.1103/PhysRevMaterials.4.034403 for additional information on DFT calculations (bulk and strained), and half-order XRD analysis.
[83] A. M. Glazer, Acta Cryst. A **31**, 756 (1975).
[84] S. J. May, J.-W. Kim, J. M. Rondinelli, E. Karapetrova, N. A. Spaldin, A. Bhattacharya, and P. J. Ryan, Phys. Rev. B **82**, 014110 (2010).
[85] W. Donner, C. Chen, M. Liu, A. J. Jacobson, Y.-L. Lee, M. Gadre, and D. Morgan, Chem. Mater. **23**, 984 (2011).